Chinese Chemical Letters 34 (2023) 108016

Contents lists available at ScienceDirect

Chinese Chemical Letters

journal homepage: www.elsevier.com/locate/cclet

Amorphous porous sulfides nanosheets with hydrophilic/aerophobic surface for high-current-density water splitting

Xiaoli Wu, Sheng Zhao, Lijie Yin, Luqi Wang, Linlin Li, Feng Hu*, Shengjie Peng*

Jiangsu Key Laboratory of Electrochemical Energy Storage Technologies, College of Materials Science and Technology, Nanjing University of Aeronautics and Astronautics, Nanjing 210016, China

ARTICLE INFO

Article history:
Received 7 August 2022
Revised 7 November 2022
Accepted 20 November 2022
Available online 25 November 2022

Keywords:
Electrocatalysts
Metal-organic frameworks
Amorphous
High current density
Overall water splitting

ABSTRACT

The rational construction of electrocatalysts with desired features is significant but challenging for superior water splitting at high current density. Herein, amorphous CoNiS nanosheets are synthesized on nickel foam (NF) through a facile structure evolution strategy and present advanced performance at high current densities in water splitting. The high catalytic activity can be attributed to the sufficient active sites exposed by the flexible amorphous configuration. Moreover, the hydrophilicity and aerophobicity of a-CoNiS/NF promote surface wettability of the self-supporting electrode and avoid the aggregation of bubbles, which expedites the diffusion of electrolyte and facilitates the mass transfer. As a result, the optimized electrode demonstrates low overpotentials of 289 and 434 mV at 500 mA/cm^2 under alkaline conditions for hydrogen evolution reaction (HER) and oxygen evolution reaction (OER), respectively. Impressively, an electrolytic water splitting cell assembled by bifunctional a-CoNiS/NF operates with a low cell voltage of 1.46 V@10 mA/cm^2 and reaches 1.79 V at 500 mA/cm^2. The strategy sheds light on a competitive platform for the reasonable design of non-precious-metal electrocatalysts under high current density.

Hydrogen with the merits of zero carbon emission and high energy density is proposed as the main carrier of future energy [1]. Electrochemical water splitting is one of the most ideal and sustainable techniques to produce hydrogen, which consists of oxygen evolution reaction (OER) at the anode and hydrogen evolution reaction (HER) at the cathode [2,3]. For overall water splitting devices, nonprecious metal-based electrocatalysts with high activity are quite necessary, which can reduce the overpotentials caused by polarization and promote the charge transfer efficiency [4–6]. Although nonprecious catalysts can work well at low current densities, their application in industrial hydrogen production at high current densities is still uncompetitive [7–9]. During large-scale catalytic hydrogen evolution, crowded gas bubbles generated on the electrode surface severely hinder the identification of the active sites, leading to attenuated durability of catalysts [10,11]. Taking gas-liquid-solid three-phase interfaces into consideration, the optimization of surface physicochemical properties has a tremendous effect on the ultimate efficiency of electrocatalysts at high current density [12,13]. The hydrophilicity of the electrode could timely facilitate the wettability of the electrocatalyst with the aqueous electrolyte, resulting in a small ohmic resistance [14,15]. Moreover, a low bubble adhesion force of the electrode surface caused by the aerophobicity is expected to contribute to buffering the accumulation of gas bubbles and avoiding the decrease of active sites caused by bubble desorption [16–19]. Consequently, the optimized non-precious catalysts with designable surface properties can effectively guarantee the direct permeation of the electrolyte and facilitate the mass transfer.

With regard to the practical industrial application, the facile synthesis and high performance of electrocatalysts at large current densities are of vital importance [20–22]. Strategies including crystallinity controlling are applied for advanced electrocatalysts, which are beneficial for electrolyzers at high current densities [23–25]. In recent years, various transition metal-based amorphous electrocatalysts have received immense research attention compared with their crystalline counterparts in terms of electrochemical water splitting at high current density [26–29]. The amorphous materials possess unique structural features of long-range disorder arrangement and short-range order, which enables better corrosion resistance and achieves confined electrocatalysis of surface as well as bulk [30]. Moreover, the defect structure offers abundant active sites and optimized adsorption energy of reaction intermediates resulting in the unusual enhancement of the intrinsic activities for HER and OER [31,32]. Normally, the amorphous phase has been continuously engineered by precursor

* Corresponding authors.
E-mail addresses: fenghu@nuaa.edu.cn (F. Hu), pengshengjie@nuaa.edu.cn (S. Peng).

https://doi.org/10.1016/j.cclet.2022.108016
1001-8417/

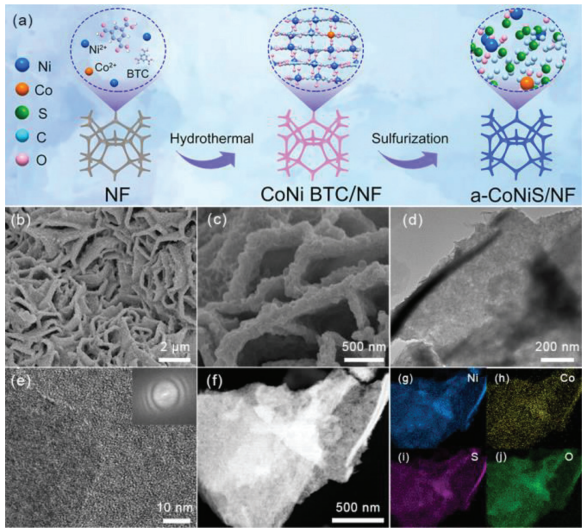

Fig. 1. (a) Illustration of the formation process of a-CoNiS/NF. Low and high magnification SEM images of (b, c) a-CoNiS/NF. (d) TEM image, (e) HRTEM image, and inset FFT figure of a-CoNiS/NF. (f) HAADF-TEM image of a-CoNiS/NF and corresponding EDS mapping images of (g) Ni, (h) Co, (i) S, and (j) O.

transformation [33–35], lattice disordering [36], and controlled hydrolysis [37] to further enhance the charge transfer capability of the pristine catalysts. Metal-organic frameworks (MOFs), featuring ultrahigh surface areas and excellent porous characteristics, usually serve as precursors for constructing well-defined amorphous catalysts [38], such as nanorods [39], nanocubes [40], and nanosheets [41]. Hierarchical porous nanosheets derived from MOF can guarantee the channels align with the direction of buoyancy to facilitate the upward movement of the gas bubbles [42]. However, electrocatalysts powder has to be fixed on a conductive substrate using polymer binders, which consequently results in significant ohmic resistance and impedes mass transportation at high current density [43]. Therefore, it is highly desirable to design electrodes with self-supporting structures and flexible configurations to facilitate mass transfer at high current densities.

Hence, we propose a chemical conversion strategy to prepare bimetallic amorphous sulfide self-supporting electrodes with versatile structures and multiple physicochemical properties. The remarkable electrocatalytic activity of the self-supporting electrodes is ascribed to the simultaneous modulation of configuration and geometric structure, as well as the systematic optimization of abundant active sites. Importantly, the synergistic effect of surface hydrophilicity and aerophobicity enhance the capacity for mass transport, thereby significantly improving the stability as well as the catalytic performance of OER and HER simultaneously. Furthermore, a-CoNiS/NF electrode water electrolyzer configured in a dual-electrode system needs only a low cell voltage of 1.46 V to reach 10 mA/cm^2 and achieves 1.79 V at 500 mA/cm^2.

The synthesis process is illustrated schematically in Fig. 1a. First, crystalline CoNi Triethylbenzene (CoNi BTC) nanorods on nickel foam were synthesized hydrothermally and used as precursors (Fig. S7 in Supporting information), followed by a ligand replacement reaction with Na_2S. Next, BTC ligands were continually leached out, causing the progressive collapse of the crystalline nanorod arrays and becoming amorphous. Simultaneously, the S^{2-} in the solution was absorbed by the positive holes through the electrostatic attraction, and the original structure was further transformed into nanosheets. Scanning electron microscopy (SEM) images show that the obtained a-CoNiS nanosheets evenly align on the substrate and exhibit excellent dispersity as demonstrated by Figs. 1b and c. Transmission electron microscopy (TEM) suggests that the external nanosheets are arranged regularly and a high degree of the roughness can be exposed (Fig. 1d). High-resolution TEM (HRTEM) exhibits no obvious lattice fringes and weak reflection halos can be distinctly observed in the corresponding fast Fourier transform (FFT) pattern, confirming the amorphous nature of the a-CoNiS/NF (Fig. 1e). The HAADF-TEM image and corresponding energy dispersive spectroscopy (EDS) elemental mapping demonstrate that Ni, Co, S, and O elements are homogeneously distributed across the entire nanosheets (Figs. 1f-j).

The crystallinity of the obtained electrocatalysts is examined by X-ray diffraction (XRD). The CoNi BTC powder is similar to the simulated CoNi BTC [44] and a-CoNiS powder do not show any apparent diffraction peaks (Fig. 2a). In Fig. 2b, Raman spectra display that the broad feature peaks of a-CoNiS/NF are centered at 450–500 cm^{-1}, which are assigned to disordered metal-S stretch mode [45]. In contrast, there are three peaks observed for the CoNi BTC, which are related to 1,3,5-triethylbenzene. The XRD patterns and Raman spectra reveal that the CoNi BTC/NF has been gradually changed into a-CoNiS/NF during the sulfurized process, suggesting the successful synthesis of amorphous configuration.

The surface chemical states of the self-supporting electrode are scrutinized by X-ray photoelectron spectroscopy (XPS). In the XPS spectra of a-CoNiS/NF, Ni shows a fairly broad Ni $2p_{3/2}$ peak at around 855.2 eV, which shifts negatively with the treatment of sulfurization, indicating a valence change caused by the activation process (Fig. 2c) [46]. From Co 2p spectrum, both a-CoNiS/NF and CoNi BTC/NF show the Co $2p_{3/2}$ peak at 781.3 eV corresponds to the Co^{2+}. It is deduced that most of the Ni−O and Co−O bonds in precursor are broken by the violent reaction process, leading to the reconstruction of metal-S species (Fig. 2d). Sulfur element with the lower electronegativity compared with oxygen exhibits weak electron-withdrawing capability, which takes responsibility for the peaks to shift negatively [47]. From Fig. 2e, the high-magnification S 2p spectrum is deconvoluted into four peaks, including S $2p_{1/2}$ (164.0 eV) and S $2p_{3/2}$ (162.5 eV), while S−O bond observed at 166–173 eV indicates the surface absorption of oxygen with sulfur [48]. Moreover, the O 1s XPS profiles of a-CoNiS/NF and CoNi BTC/NF can be fitted into three distinct peaks, which are assigned to chemical oxygen-metal (OI at 531.0 eV), oxygen vacancies (OII at 531.5 eV), surface-adsorbed or OH species (OIII at 533.4 eV) (Fig. 2f) [49]. With the wet-chemical reaction, the oxygen vacancies are formed and the S^{2-} is absorbed by the positive holes through the electrostatic attraction, which is beneficial for the electron transfer [50].

The activity of the as-prepared electrocatalysts was measured in 1.0 mol/L KOH aqueous solution. As displayed in Fig. 3a, porous nanosheet a-CoNiS/NF electrode exhibits significantly improved OER activity with ultralow overpotentials of 183 and 434 mV at 10 and 500 mA/cm^2, which outperform that of CoNi BTC/NF (212 and 507 mV) and the benchmark RuO_2 (308 mV at 10 mA/cm^2). Analogously, the overpotentials of a-CoNiS/NF are only 73 and 289 mV for HER at 10 and 500 mA/cm^2, which are considerably smaller than that of CoNi BTC/NF (155 and 564 mV). Tafel slope is a vital parameter to evaluate the underlying reaction kinetics [51]. The Tafel slopes of CoNi BTC/NF, a-CoNiS/NF, along with commercial Pt/C for HER are 124.72, 48.15, and 36.84 mV/dec, respectively (Fig. 3b). Meanwhile, the Tafel slope of a-CoNiS/NF is 20.18 mV/dec for OER and much smaller than that of CoNi BTC/NF (25.41 mV/dec), and commercial RuO_2 (71.25 mV/dec) in alkaline media (Fig. 3c), confirming the amorphous materials as outstanding electrocatalysts with better HER and OER kinetics. According to Fig. 3d, the remarkable OER and HER activities of a-CoNiS/NF are well ahead of many bifunctional amorphous composites and transition metal sulfides in alkaline media. The activities of a-CoNiS/NF with a different stoichiometry of Co/Ni were measured (Figs. S2a and b in Supporting information) and a-CoNiS/NF with a Co/Ni

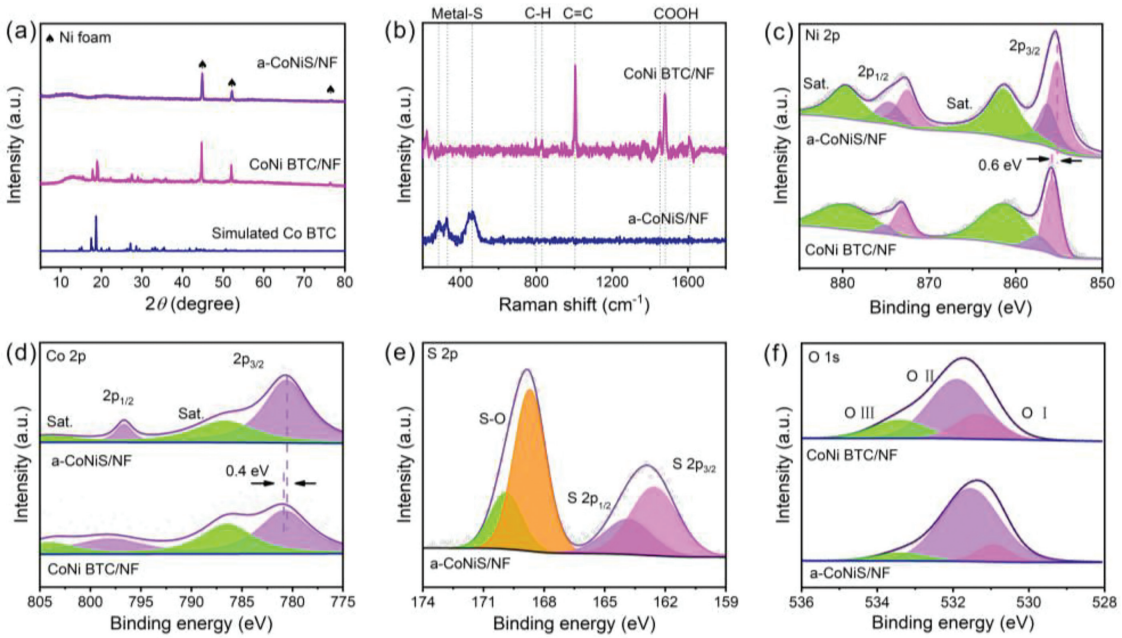

Fig. 2. (a) XRD patterns of CoNi BTC powder scraped from the Ni foam, a-CoNiS powder scraped from the Ni foam, and simulated CoNi BTC. (b) Raman spectra of CoNi BTC/NF, and a-CoNiS/NF; High-resolution XPS spectra of (c) Ni 2p, (d) Co 2p, (e) S 2p, (f) O 1s in CoNi BTC/NF and a-CoNiS/NF, respectively.

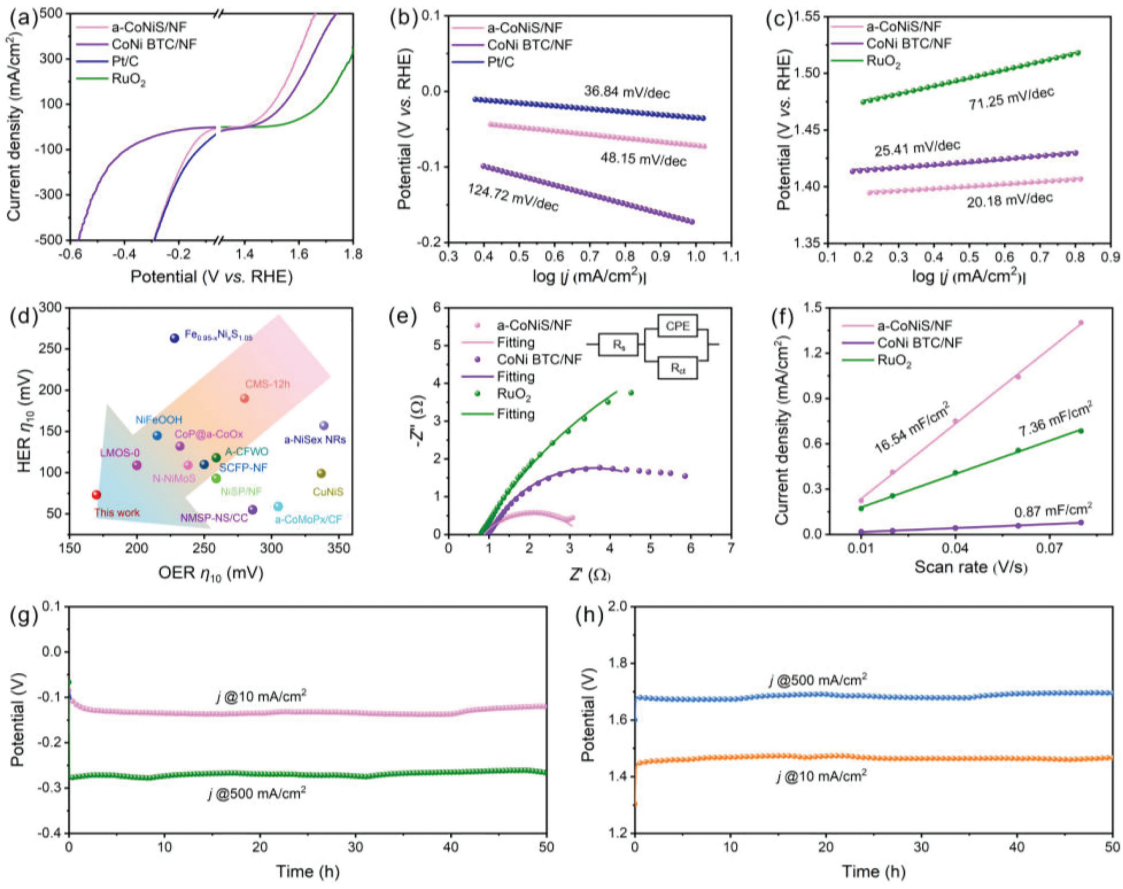

Fig. 3. Electrochemical performance of HER and OER in 1 mol/L KOH. (a) HER and OER polarization curves of a-CoNiS/NF, CoNi BTC/NF, Pt/C, and RuO_2 with iR compensation. (b, c) Corresponding Tafel slopes of HER and OER. (d) Comparison of the overpotentials for OER and HER at 10 mA/cm^2 of a-CoNiS/NF with other reported amorphous or sulfides electrocatalysts. (e) Nyquist curves of a-CoNiS/NF, CoNi BTC/NF, and RuO_2 for OER. (f) C_{dl} measurements of a-CoNiS/NF, CoNi BTC/NF, and RuO_2. (g, h) Stability curves of a-CoNiS/NF at the constant current densities of 10 and 500 mA/cm^2 for HER and OER.

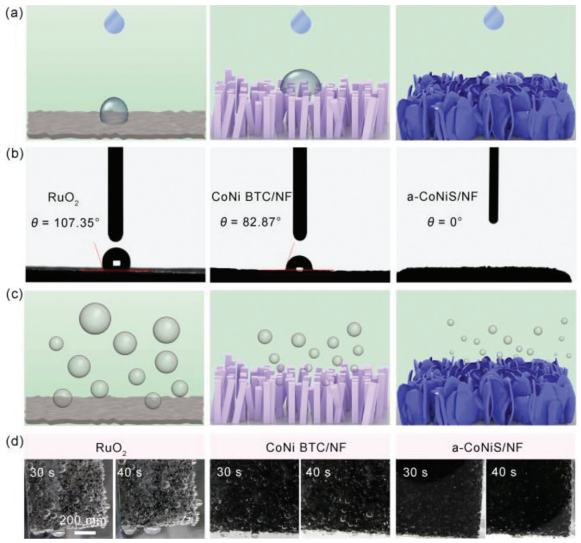

Fig. 4. (a) Schematics of the "hydrophilicity" feature of RuO_2, CoNi BTC/NF, and a-CoNiS/NF. (b) Bubble contact angle images of RuO_2, CoNi BTC/NF, and a-CoNiS/NF. (c) Schematics display the "superaerophobic" feature of RuO_2, CoNi BTC/NF, and a-CoNiS/NF. (d) The bubble evolution processes on the surface of RuO_2, CoNi BTC/NF, and a-CoNiS/NF.

ratio of 1:10 demonstrates the maximum activity. We further acquired crystalline-CoNiS/NF (denoted as c-CoNiS/NF) and tested its catalytic capability. The XRD pattern of c-CoNiS/NF (Fig. S3 in Supporting information) displays characteristic peaks corresponding to Ni_3S_2 (JCPDS No. 8–126) and the morphology of c-CoNiS/NF converts into particles. The polarization curves demonstrate that the HER and OER performance of c-CoNiS/NF is inferior to that of a-CoNiS/NF, indicating that the amorphous structure precedes its crystalline counterparts (Figs. S4-S6 in Supporting information).

Moreover, electrochemical impedance spectroscopy (EIS) was performed to verify the interfacial kinetics between the electrocatalyst and electrolyte [52]. From EIS Nyquist curves, the R_{ct} of a-CoNiS/NF is smaller than that of other electrocatalysts in an alkaline medium (Fig. 3e and Fig. S9 in Supporting information). The lowest R_{ct} value of a-CoNiS/NF disclosed faster electron transfer and favorable kinetics, which is consistent with the ultralow overpotential and small Tafel plots for a-CoNiS/NF. As displayed in Fig. S10 (Supporting information), the C_{dl} is determined by CV curves with different scan rates (10–80 mV/s) to explore the electrochemical active area (ECSA) of a-CoNiS/NF. The C_{dl} value of a-CoNiS/NF is 16.54 mF/cm^2, much larger than that of RuO_2 (7.36 mF/cm^2) and CoNi BTC/NF (0.87 mF/cm^2) in the alkaline condition (Fig. 3f). Therefore, it is deduced that the amorphous configuration caused by sulfurization favors the distribution of active components and the enlargement of the ECSA. The intimate contact of electrolyte with well-exposed active sites may accelerate the mass transfer, further improving electrocatalytic performances under high current density. The long-term stability of a-CoNiS/NF for HER and OER is another crucial factor that evaluates the promotability to the commercial level large-scale. Through continuously running at the current density of 10 and 500 mA/cm^2 (Figs. 3g and h), the chronopotentiometry curves of a-CoNiS/NF for HER and OER show no signs for 50 h, which substantiates the remarkable electrochemical stability and indicates the superiority at high current density.

Contact angles are measured to manifest the wettability of the surface. Fig. 4a exhibits the schematic diagram for the hydrophilic transformation of RuO_2, CoNi BTC/NF, and a-CoNiS/NF. The contact angles of the above samples are 107.35°, 82.87°, and 0° (Fig. 4b), respectively. It is of vital importance to understand the mass transfer processes in HER and OER under high current density that contribute to the electrochemical conversion for gas evolution reactions at the electrode-electrolyte interface. The hydrophilicity of the electrode surface affects electrolyte permeation that determines the reaction kinetics [53,54]. Moreover, the droplet is rapidly absorbed by the electrode surface of a-CoNiS/NF, which is recorded in Movie S1 (Supporting information). It is deduced that the best wettability of a-CoNiS/NF is attributed to its amorphous architecture with open vacancy, which is expected to facilitate electrolyte reaching active catalytic sites [55,56]. Furthermore, according to Le Chatelier's principle, air bubbles are released rapidly [57], which will buffer the volume expansion induced by bubble desorption as well as accelerate the reaction kinetics. Benefiting from the superaerophobic property of the a-CoNiS/NF electrode, O_2 bubbles generate and instantly emancipate from the electrode according to Fig. 4c. A camera is conducted to record the bubble evolution process and size distribution during the OER at a current density of 500 mA/cm^2 (Fig. 4d). On the electrodes of RuO_2 and CoNi BTC/NF, tiny bubbles generate slowly and then grow large enough to escape the electrode smoothly. In principle, it is better to form uniform O_2 bubbles that provide a larger contact angle and smaller diameter, which may facilitate rapid release from the catalyst surface [58,59]. Thus, the bubbles on the electrode surface with a smaller stretch force can depart from the electrode without shielding a large area of the active sites, thereby retaining stability at high current density.

Figs. 5a and b display the proposed HER and OER reaction paths of a-CoNiS/NF. The scheme demonstrates that OER requires four elementary reaction steps, which undergo a continuous cycle of oxidation from the adsorption of a water molecule to the evolution of dioxygen [60,61]. In the case of HER, the Tafel slope of a-CoNiS/NF follows the relatively slower Volmer-Heyrovsky mechanism. Raman spectra is used to investigate the composition of a-CoNiS/NF after stability (Fig. 5c). New characteristic peaks at 247 cm^{-1} and 327 cm^{-1} assigned to the vibration mode of crystalline Ni_3S_2 are detected during the HER process [62]. The Raman spectra of a-CoNiS/NF after OER indicate that the vibrations of Metal−S bonds are maintained well after long-term stability, and a new band at 554 cm^{-1} for Ni−O vibrations in $Ni(OH)_2$ is attributed to the oxidation of nickel [63]. Moreover, XPS spectra in Fig. 5d show that part of the nickel in a-CoNiS/NF is reduced to bivalent metallic states during the HER process, resulting from the direct reduction of trivalent metal oxides to active sites [64,65]. The Co 2p XPS spectra after water splitting are nearly unchanged (Fig. 5e). Due to the relatively stable structure of the amorphous bimetallic sulfide, the intensities of the S 2p spectrum in the a-CoNiS/NF after HER do not decrease significantly compared with the original sample (Fig. 5f), further indicating the sulfide is the true active site [66]. In another regard, the valence state of the a-CoNiS/NF electrode after the OER test shows negligible changes, which reveals the superior properties of amorphous Ni-S after long-term stability tests. Therefore, it is inferred that the final partial transformation of amorphous metal sulfides into metal oxides may contribute to the high stability of the a-CoNiS/NF electrode.

Based on the superior electrochemical performance for HER and OER, a-CoNiS/NF was used as an efficient and stable bifunctional electrode for overall water splitting. As shown in Fig. 6a, a-CoNiS/NF‖a-CoNiS/NF achieves a low cell voltage of 1.46 V to reach a current density of 10 mA/cm^2, which is lower than that of Pt/C‖RuO_2 (1.60 V) and CoNi BTC/NF‖CoNi BTC/NF‖BTC/NF (1.67 V). To further evaluate the stability of a-CoNiS/NF‖a-CoNiS/NF (Fig. 6b), the LSV polarization curves of a-CoNiS/NF‖a-CoNiS/NF before and after 500 cycles are recorded, and only a slightly negative shift is observed, indicating the high stability. Furthermore, a-CoNiS/NF is used to establish an H-type cell with separated electrodes by a proton exchange membrane, while the assembled electrolyzer quantifies the energy conversion efficiency during electrocatalytic

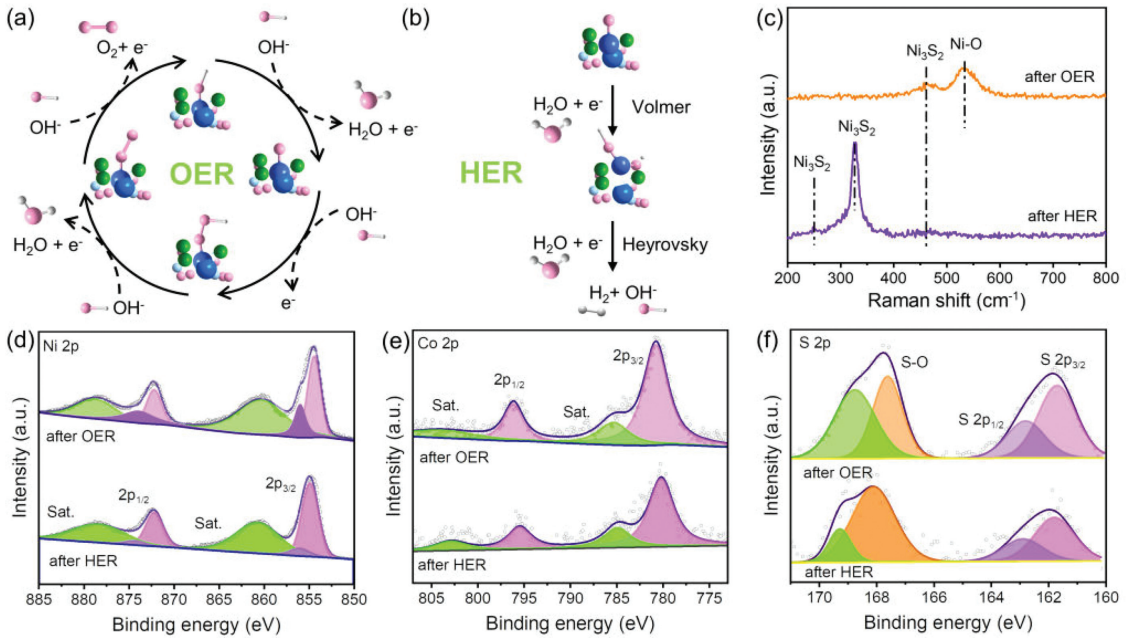

Fig. 5. Scheme of the transition state in the mechanism of (a) OER and (b) HER at a-CoNiS/NF. (c) Raman spectra of a-CoNiS/NF after HER and OER. XPS fine spectra of (d) Ni 2p, (e) Co 2p, and (f) S 2p for a-CoNiS/NF after HER and OER.

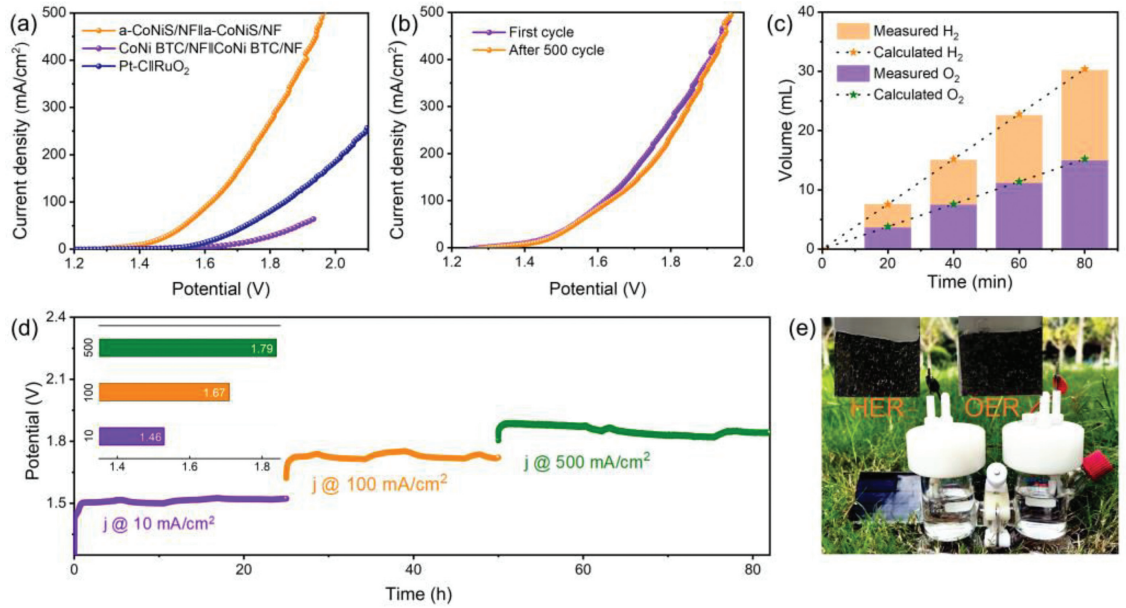

Fig. 6. (a) Overall water splitting polarization curves of a-CoNiS/NF||a-CoNiS/NF, CoNi BTC/NF||CoNi BTC/NF, and Pt-C||RuO_2 in 1 mol/L KOH without iR-compensation. (b) LSV before and after successive CV scanning for 500 cycles at a scan rate of 1 mV/s of a-CoNiS/NF||a-CoNiS/NF. (c) A diagram of Faraday efficiency for a-CoNiS/NF||a-CoNiS/NF. (d) Chronopotentiometric curves of a-CoNiS/NF||a-CoNiS/NF at various current densities and overpotentials at different current densities in detail (inset). (e) Actual operation device of a-CoNiS/NF||a-CoNiS/NF for water splitting derived by the 1.5 V solar cell panel as well as the anode and cathode with evolved O_2 and H_2, respectively.

water splitting. The plots of gas volume *versus* time are given in Fig. 6c, and the experimentally evolved molar ratio of O_2 to H_2 is close to the theoretical stoichiometry of l:2 for overall water splitting. This reveals that the cell constructed by a-CoNiS/NF possesses the Faraday efficiency of nearly 100%.

In addition, the long-term stability of a-CoNiS/NF||a-CoNiS/NF was tested at constant current densities of 10, 100, and 500 mA/cm^2 (Fig. 6d). Multi-step chronopotentiometry curve shifts slightly after running for over 80 h, further showing the mechanical robustness of the electrode. Notably, the inset picture in Fig. 6e displays the potentials obtained from different current densities, manifesting the optimal catalytic activity for overall water splitting. Benefiting from the outstanding performances of a-CoNiS/NF, a device is assembled to convert solar energy into electric energy to drive overall water splitting (Fig. 6e). The inset in Fig. 6e displays that the H_2 and O_2 bubbles are rapidly generated from anode and cathode, indicating that the rational design of non-precious-metal electrocatalysts provides a chance for practical applications of H_2 production using the commercial portable battery.

In conclusion, we successfully synthesized bifunctional electrocatalysts by transforming crystal CoNi BTC into amorphous CoNiS nanosheets for both HER and OER. Notably, the obtained electrode leverages multiple advantages of amorphous configuration, geometric structure, and superior hydrophilic/superaerophobic surface

to demonstrate remarkably low overpotentials and long-term durability for electrocatalysis. Combined with the high mass transport through the nanosheets, a-CoNiS/NF reveals low overpotentials of 289 and 434 mV at 500 mA/cm^2 and maintains excellent stability for 50 h towards both OER and HER. Meanwhile, the alkaline electrolyzer assembled by a-CoNiS/NF has an excellent overall water-splitting output (1.46 V@10 mA/cm^2 and 1.79 V@500 mA/cm^2), outperforming many reported amorphous electrodes. Given the amorphous hierarchical porous nanosheet structure as a typical model, the strategy could open up new ways for the development of energy conversion applications.

Declaration of competing interest

The authors declare that they have no known competing financial interests or personal relationships that could have appeared to influence the work reported in this paper.

Acknowledgments

This work was supported by the National Natural Science Foundation of China (Nos. 51871119, 22101132, and 22075141), Scientific and Technological Innovation Special Fund for Carbon Peak and Carbon Neutrality of Jiangsu Province (No. BK20220039), Jiangsu Provincial Founds for Natural Science Foundation (No. BK20210311), China Postdoctoral Science Foundation (Nos. 2018M640481 and 2019T120426), the Natural Science Foundation of Jiangsu Province (No. BK20210311), Jiangsu Postdoctoral Research Fund (No. 2019K003), and the Postgraduate Research & Practice Innovation Program of NUAA (No. xcxjh20210607).

Supplementary materials

Supplementary material associated with this article can be found, in the online version, at doi:10.1016/j.cclet.2022.108016.

References

[1] K. Hu, T. Ohto, Y. Nagata, et al., Nat. Commun. 12 (2021) 203.
[2] H. Yang, M. Driess, P.W. Menezes, Adv. Energy Mater. 11 (2021) 2102074.
[3] L. Sun, Q. Luo, Z. Dai, F. Ma, Coordin, Chem. Rev. 444 (2021) 214049.
[4] Y.C. Zhang, C. Han, J. Gao, et al., ACS Catal. 11 (2021) 12485–12509.
[5] X. Liu, M. Gong, S. Deng, et al., Adv. Funct. Mater. 31 (2021) 2009032.
[6] L. Deng, F. Hu, M. Ma, et al., Angew. Chem. Int. Ed. 60 (2021) 22276–22282.
[7] Y. Tan, R. Xie, S. Zhao, et al., Adv. Funct. Mater. 31 (2021) 2105579.
[8] C. Song, Z. Zhao, X. Sun, et al., Small 15 (2019) 1804268.
[9] Y. Song, K. Ji, H. Duan, M. Shao, Exploration 1 (2021) 20210050.
[10] Z. Chen, M. Ju, M. Sun, et al., Angew. Chem. Int. Ed. 60 (2021) 9699–9705.
[11] A. Huang, Y. Ma, J. Peng, et al., eScience 1 (2021) 141–162.
[12] X. Lu, C. Zhao, Nat. Commun. 6 (2015) 6616.
[13] X. Shan, J. Liu, H. Mu, et al., Angew. Chem. Int. Ed. 59 (2020) 1659–1665.
[14] Y. Ko, J. Park, J. Mo, et al., Adv. Funct. Mater. 31 (2021) 2102530.
[15] H. Liu, X. Li, L. Chen, et al., Adv. Funct. Mater. 32 (2021) 2107308.
[16] Q. Zhang, W. Xiao, W.H. Guo, et al., Adv. Funct. Mater. 31 (2021) 2102117.
[17] C.T. Hsieh, C.L. Huang, Y.A. Chen, S.Y. Lu, Appl. Catal. B: Environ. 267 (2020) 118376.
[18] Y. Song, J. Cheng, J. Liu, et al., Appl. Catal. B: Environ. 298 (2021) 120488.
[19] L. Li, D. Yu, P. Li, et al., Energ. Environ. Sci. 14 (2021) 6419–6427.
[20] X. Zou, Y. Liu, G.D. Li, et al., Adv. Mater. 29 (2017) 1700404.
[21] X. Li, C. Liu, Z. Fang, et al., Small 18 (2022) 2104354.
[22] X. Guo, X. Wan, Q. Liu, et al., eScience 2 (2022) 304–310.
[23] S. Anantharaj, S. Noda, Small 16 (2020) 1905779.
[24] S. Jiao, Z. Yao, M. Li, et al., Nanoscale 11 (2019) 18894–18899.
[25] Y. Sun, S. Xu, C.A. Ortíz Ledón, et al., Exploration 1 (2021) 20210021.
[26] L. Yang, Z. Guo, J. Huang, et al., Adv. Mater. 29 (2017) 1704574.
[27] H. Song, J. Yu, Z. Tang, et al., Adv. Energy Mater. 12 (2022) 2102573.
[28] G. Chen, Y. Zhu, H.M. Chen, et al., Adv. Mater. 31 (2019) 1900883.
[29] W. Yuan, S. Wang, Y. Ma, et al., ACS Energy Lett. 5 (2020) 692–700.
[30] L. Zhang, W. Cai, N. Bao, Adv. Mater. 33 (2021) 2100745.
[31] H. Huang, A. Cho, S. Kim, et al., Adv. Funct. Mater. 30 (2020) 2003889.
[32] L. Gao, Z. Yang, T. Sun, et al., Adv. Energy Mater. 12 (2022) 2103943.
[33] Y. Cao, Y. Zhu, C. Du, et al., ACS Nano 16 (2022) 1578–1588.
[34] B. Liu, L. Wang, Y. Zhu, et al., ACS Nano 16 (2022) 12900–12909.
[35] W. Younas, M. Naveed, C. Cao, et al., J. Colloid Interface Sci. 608 (2022) 1005–1014.
[36] D. Li, Y. Qin, J. Liu, et al., Adv. Funct. Mater. 32 (2022) 2107056.
[37] H. Sun, L. Chen, Y. Lian, et al., Adv. Mater. 32 (2020) 2006784.
[38] D. Chen, L. Wei, J. Li, Q. Wu, J. Energy Storage 30 (2020) 101525.
[39] H.J. Lee, J. We, J.O. Kim, et al., Angew. Chem. Int. Ed. 54 (2015) 10564–10568.
[40] P. Cai, J. Huang, J. Chen, Z. Wen, Angew. Chem. Int. Ed. 56 (2017) 4858–4861.
[41] W. Zhao, Y. Zheng, L. Cui, et al., Chem. Eng. J. 371 (2019) 461–469.
[42] D. Senthil Raja, X.F. Chuah, S.Y. Lu, Adv. Energy Mater. 8 (2018) 1801065.
[43] T. Kou, S. Wang, R. Shi, et al., Adv. Energy Mater. 10 (2020) 2002955.
[44] J.F. Lu, Z.H. Liu, Polyhedron 107 (2016) 19–26.
[45] C.F. Wen, M. Zhou, P.F. Liu, et al., Angew. Chem. Int. Ed. 61 (2021) 111700.
[46] W. Lu, X. Li, F. Wei, et al., Electrochim. Acta 318 (2019) 252–261.
[47] Z. Wang, G. Qian, T. Yu, et al., Chem. Eng. J. 434 (2022) 134669.
[48] J. Song, S. Qiu, F. Hu, et al., Adv. Funct. Mater. 31 (2021) 2100618.
[49] H. Wang, F. Yin, N. Liu, et al., ACS Sustain. Chem. Eng. 9 (2021) 4509–4519.
[50] K. Zhu, F. Shi, X. Zhu, W. Yang, Nano Energy 73 (2020) 104761.
[51] Y. Hao, F. Hu, Y. Chen, et al., Adv. Fiber Mater. 4 (2022) 185–202.
[52] F. Hu, D. Yu, M. Ye, et al., Adv. Energy Mater. 12 (2022) 2200067.
[53] H. Liu, X. Li, L. Chen, et al., Adv. Funct. Mater. 32 (2022) 2107308.
[54] Y.K. Li, G. Zhang, W.T. Lu, F.F. Cao, Adv. Sci. 7 (2020) 1902034.
[55] X. Qin, B. Yan, D. Kim, et al., Appl. Catal. B: Environ. 304 (2021) 120923.
[56] F. Zhang, R. Ji, Y. Liu, et al., Appl. Catal. B: Environ. 276 (2020) 119141.
[57] M.B. Wu, C. Zhang, Y. Xie, et al., ACS Appl. Mater. Interfaces 13 (2021) 51039–51047.
[58] L. Wan, Z. Xu, P. Wang, et al., Chem. Eng. J. 431 (2022) 133942.
[59] W. Liu, X. Wang, F. Wang, et al., Nat. Commun. 12 (2021) 6776.
[60] H. Huang, D. Yu, F. Hu, et al., Angew. Chem. Int. Ed. 61 (2022) e202116068.
[61] P. Zhai, Y. Zhang, Y. Wu, et al., Nat. Commun. 11 (2020) 5462.
[62] K. Wan, J. Luo, C. Zhou, et al., Adv. Funct. Mater. 29 (2019) 1900315.
[63] M.W. Louie, A.T. Bell, J. Am. Chem. Soc. 135 (2013) 12329–12337.
[64] H. Su, M.A. Soldatov, V. Roldugin, Q. Liu, eScience 2 (2022) 102–109.
[65] C. Huang, L. Yu, W. Zhang, et al., Appl. Catal. B: Environ. 276 (2020) 119137.
[66] T.L.L. Doan, D.T. Tran, D.C. Nguyen, et al., Adv. Funct. Mater. 31 (2021) 2007822.